



Cite this: *Digital Discovery*, 2024, **3**, 919

Repurposing quantum chemical descriptor datasets for on-the-fly generation of informative reaction representations: application to hydrogen atom transfer reactions[†]

Javier E. Alfonso-Ramos, ^a Rebecca M. Neeser ^{bc} and Thijs Stuyver ^{*,a}

In this work, we explore how existing datasets of quantum chemical properties can be repurposed to build data-efficient downstream machine learning models, with a particular focus on predicting the activation energy of hydrogen atom transfer (HAT) reactions. Starting from a valence bond (VB) analysis of a generic HAT process, a set of informative descriptors is identified. Next, a surrogate neural network model is constructed to predict an informative representation, based on the identified VB descriptors, with the help of a publicly available dataset of (pre-computed) quantum chemical properties of organic radicals. We demonstrate that coupling the resulting on-the-fly informative representation to a secondary machine-learning model for activation energy prediction outperforms various predictive model architectures starting from conventional machine-learning inputs by a wide margin, at no additional computational cost. By basing their final predictions on physically meaningful descriptors, our models enable the extraction of chemical insights, providing an additional benefit. Finally, because of the extreme data efficiency of our descriptor-augmented models, we are able to fine-tune and apply them to small datasets across various reaction conditions, settings and application domains, ranging from regular (liquid phase) synthesis, over metabolism and drug design, to atmospheric chemistry.

Received 13th February 2024
Accepted 29th March 2024

DOI: 10.1039/d4dd00043a
rsc.li/digitaldiscovery

1 Introduction

In recent years, the interest in predictive (machine learning) models for chemical reactivity has soared. For tasks for which hundreds of thousands to millions of data points are available, *e.g.*, forward and retrosynthesis prediction, significant strides towards accurate machine learning (ML) models have been made.^{1–7} In the absence of data scarcity, neural network architectures that learn from simple structural descriptions of molecules can be adapted to these respective tasks with great success. For example, both graph neural networks (GNNs) operating on 2D molecular graphs and Transformer models operating on Simplified Molecular Input Line Entry Specification (SMILES)⁸ strings can be trained to predict the main product of chemical reactions with roughly 90% accuracy on the popular USPTO benchmark dataset.^{1–3}

For more specialized reactivity tasks (the prediction of activation energies/reaction rates, yields, enantiomeric excess *etc.*), however, data tend to be scarce, and often number in the hundreds rather than in the hundreds of thousands. A straightforward application of the same type of data-hungry model architectures is generally not feasible in these cases, as training these models from scratch means that they must learn how to properly interpret a molecular structure. One potential approach to improve the data efficiency of machine learning models is introducing domain knowledge about the underlying physics/quantum chemistry into the model. Models starting from physically meaningful input representations, *i.e.*, representations based on quantum mechanical (QM) reactivity descriptors, have been demonstrated to reach reasonable accuracy for datasets consisting of only a couple hundred or a few thousand data points,^{9–18} and they have been reported to be significantly more generalizable, *i.e.*, they are significantly more accurate in out-of-sample predictions, than conventional, structure/graph-based, analogs.^{11,12,19}

Unfortunately, QM descriptors tend to be computationally expensive – since they typically involve an elaborate workflow consisting of conformer generation, geometry optimization and finally a single-point density functional theory (DFT) calculation for each unique molecule – limiting their applicability in broad virtual screening campaigns. A promising strategy to circumvent this limitation is to use separate machine learning models

^aEcole Nationale Supérieure de Chimie de Paris, Université PSL, CNRS, Institute of Chemistry for Life and Health Sciences, 75 005 Paris, France. E-mail: thijs.stuyver@chimieparistech.psl.eu

^bMassachusetts Institute of Technology, Department of Chemical Engineering, 02139 Cambridge, MA, USA

^cETH Zürich, Institute of Pharmaceutical Sciences, 8093 Zürich, Switzerland

† Electronic supplementary information (ESI) available. See DOI: <https://doi.org/10.1039/d4dd00043a>



to predict these QM reactivity descriptors on-the-fly, starting from a simple 2D (graph) or geometry-based representation. Some prominent examples of such descriptor prediction models are Chemprop, DeepMoleNet, SchNet and AIMNet.^{20–23} In 2020, Guan *et al.* proposed to directly integrate such a descriptor prediction model into a reactivity prediction model as a surrogate.²⁴ In their approach, a directed message-passing neural network (D-MPNN) model²⁰ was trained to predict various atom- and bond-level QM descriptors from input molecular structures. These QM descriptors were subsequently used to augment the hidden representations of a Weisfeiler–Lehman (WL) based GNN²⁵ to predict regiochemical preferences for (aromatic) substitution reactions. For training sets as small as 200 data points, the resulting “QM-augmented” models reached accuracies of 85% and more on a random data split, outperforming regular GNN analogs by more than 10%. Furthermore, the developed models were extremely fast; individual predictions required 100 ms or less, implying that they could be readily employed in high-throughput screening campaigns. In a follow-up study, Stuyver *et al.* adapted this model to predict activation energies for competing (gas-phase) E₂ and S_N2 reactions^{26,27} and observed a remarkable improvement in accuracy for their GNN model upon QM-augmentation as well, particularly in the data-limited regime.²⁸ It should be noted that the inclusion of a surrogate model for QM-derived descriptors has also recently been tried – with success – for the prediction of ADME properties for candidate drug molecules.²⁹

Even when a surrogate model strategy is viable, initial training data for the model still needs to be generated, and in some situations, this may actually be more expensive than the explicit calculation of QM descriptors at inference time. For example, in their proof of principle study, Guan *et al.*²⁴ generated a dataset of selected QM properties for 130k organic molecules, extracted from the ChEMBL³⁰ and Pistachio³¹ databases.

A potential strategy to circumvent the expensive QM descriptors calculations altogether would be to use pre-existing datasets. In recent years, various general-purpose public datasets of computed QM properties of molecules have been released.^{32–38} While these datasets have found dual use as benchmarking targets,^{39–41} as well as training data for generative models,^{42–44} their repurposing for (indirectly related) downstream predictive tasks, *e.g.*, the prediction of chemical reactivity, has remained largely unexplored up to this point.

Here, we will demonstrate that such a data repurposing strategy can be readily applied to efficiently learn activation energies for hydrogen atom transfer (HAT) reactions. Starting from a generic description of HAT reactivity within the valence bond perspective, we determine a set of qualitative characteristics that can be expected to capture the main trends for this type of reactivity. Based on this analysis, we identify the recently released dataset of QM properties for 40 000 closed-shell organic molecules and 200 000 radical analogs by Paton and co-workers, BDE-db,³⁶ as a useful source of informative descriptors and build a surrogate model able to infer these descriptors on the fly across a broad chemical reaction space based on a simple SMILES string input.³⁶ The QM representation emerging from this surrogate model is subsequently demonstrated to outperform traditional structure-based representations for various machine learning

model architectures on a challenging, in-house generated dataset of diverse hydrogen abstraction reactions by a large margin. Most importantly, models based on the developed surrogate QM representation are extremely data efficient, approaching convergence for training dataset sizes of only a couple hundred points.

Finally, we demonstrate the practical usefulness of the developed representation by considering various real-world applications. HAT reactivity plays a central role in various sub-fields of chemistry. For example, HAT reactions constitute the starting point of many oxidation pathways in polymer, atmospheric and combustion chemistry.^{45–50} Additionally, they are key transformations giving rise to the breakdown of active pharmaceutical ingredients, so their kinetic and thermodynamic properties facilitate the prediction of the stability of these compounds,^{51,52} as well as the formation of potentially hazardous metabolites.⁵³ Finally, HAT reactions also play a central role in various common synthesis strategies, *e.g.* in several flavors of C–H functionalization and photocatalysis, and a lot of effort has been devoted to gaining insights into the factors that affect their rates and yields.^{54–58} As a result, several small datasets have been produced for this reaction class in recent years, each with distinct reaction scopes and conditions, depending on the specific application for which they were designed.^{45,53,57,59–65} Because of their heterogeneity, these datasets cannot be combined easily. As will be demonstrated below, with our extremely data-efficient model architectures, we are able to meaningfully learn from these small datasets, and generate accurate predictions across the chemical spaces associated with the respective application domains, at both an unprecedented speed and an extremely low computational cost.

In essence, the proposed strategy rests on making the overall machine learning model architecture modular, with a core informative representation prediction part, followed by a fairly linear and extremely data-efficient downstream reactivity model part, that can be easily retrained on/fine-tuned to the specific application or dataset at hand. It should be noted that the presented strategy can also be regarded as an alternative to the more conventional approach of fine-tuning pre-trained models by modifying the prediction head.⁶⁶ Overall, we believe that the presented work provides a blueprint for how – starting from physics/chemistry-inspired mechanistic insights – useful (existing) datasets of QM properties can be identified and leveraged for downstream predictive tasks. Furthermore, it underscores the importance of community efforts to generate and curate QM property datasets – and to include as many informative descriptors as possible in them. At the end of this contribution, we briefly reflect on the transferability of the approach to other reaction types.

2 The valence bond reactivity model as a source of inspiration for descriptor selection

As indicated in the introduction, to gain qualitative insights into the main factors driving HAT reactivity, we took inspiration from qualitative Valence Bond (VB) theory.^{67,68} In a VB reactivity



analysis, reactivity diagrams, reflecting the shape of the potential energy surface (PES) associated with a given chemical system along a chosen reaction coordinate, are constructed. Usually, one starts by examining the evolution of the so-called “diabatic curves”, which represent the wave function associated with a limited number of VB structures; *i.e.*, they correspond to a localized VB configuration (*e.g.*, a specific Lewis structure of the reactants or products). These individual diabatic curves interact along the reaction coordinate, and collectively they give rise to the “adiabatic” curve, *i.e.*, the full ground-state PES associated with the chemical system under consideration. The transition state then corresponds to the top of the hill of the adiabatic state, which usually lies in the same region as the crossing point between the reactant and product diabatic states. An in-depth discussion of the theory behind the construction VB reactivity diagrams is provided in ref. 68. In Fig. 1, a simplified sketch of such a diagram is presented for the model reaction between H_2 and H^+ .

From a generic valence bond diagram, the following universally valid – yet approximate – expression for the barrier height can be derived:⁶⁸

$$\Delta E = f \times (G_r + G_p) + \frac{1}{2} \Delta E_{rp} + B \quad (1)$$

where G_r is the promotion energy on the reactant side, *i.e.*, the energy difference between the reactant and product diabatic states in the reactant geometry, G_p is the corresponding promotion energy on the product side, f depends on the curvature of the diabatic states and is a fraction, *i.e.*, a number

between 0 and 1, and ΔE_{rp} corresponds to the thermodynamic driving force, *i.e.*, the energy difference between reactants and products. These first two terms in the expression collectively indicate the height of the crossing point between the reactant and product diabatic states. The third and final term, B , is a correction term corresponding to the interaction between the diabatic states in the transition state geometry, *i.e.*, it corresponds to the energy lowering from the crossing point of the reactant and product diabatic states and the top of the hill on the adiabatic state.

Eqn (1) is an essentially linear – and inherently interpretable – one, and has been applied successfully to various areas of chemical reaction space, leading to robust and fairly accurate barrier estimates.^{69–76} Unfortunately, obtaining reliable values for each of the featured parameters is ambiguous and computationally expensive for some reaction types. For HAT reactions, however, most of the terms in the expression can straightforwardly be connected to unambiguous QM descriptors, which can be readily computed with high accuracy, hence our decision to focus on this type of reactivity in this proof of concept study.

More specifically, in HAT reactions, the promotion energies, G_r and G_p , are proportional to the vertical/frozen bond dissociation energy (BDE) – or, more accurately, the bond dissociation free energy (BDFE) – of the covalent bond being broken in the reactant and product geometries respectively.⁶⁸ The thermodynamic driving force, ΔE_{rp} , in its turn corresponds to the (relaxed) BD(F)E by definition. f and B have been demonstrated to be fairly constant within narrow reaction families, *e.g.*, when considering a carbon-based radical abstracting H atoms from a C sp^3 bond.⁶⁸ Since our ambition here is to generalize across the full space of (neutral) C, H, N, O containing organic radical reactions, this assumption can be expected not to hold perfectly. It has been demonstrated however that both of these parameters are connected to a variety of descriptors that can in fact be quantified straightforwardly.

First and foremost, f depends on the electrostatic interactions along the abstraction site–hydrogen–radical site point-charge array in the transition state (TS) geometry, which can be probed indirectly by considering atomic charges (in the reactant and product geometries).⁷⁷ Additionally, f also depends on the sterics around the radical and abstraction sites – steric bulk around those sites can be expected to strain the transition state geometry and hence should result in a higher crossing-point between the reactant and product diabatic curves. Commonly, buried volume (V_{bur}) is used as a descriptor to quantify steric bulk around reactive sites.⁷⁸ Finally, f has also been suggested to depend on the extent of delocalization in reactant and product, which can be probed through consideration of the spin density (ρ).⁶⁸ However, an alternative viewpoint is that losses and/or gains in delocalization energy may already be fully reflected in the thermodynamic driving force term (ΔE_{rp}), so that the impact of delocalization on f may actually be negligible.⁷³ As indicated above, B depends on the interaction between the various diabatic states, and has been connected primarily to the (local) ionization potentials and electron affinities – and/or electron negativities – at the radical/abstraction sites.⁶⁸

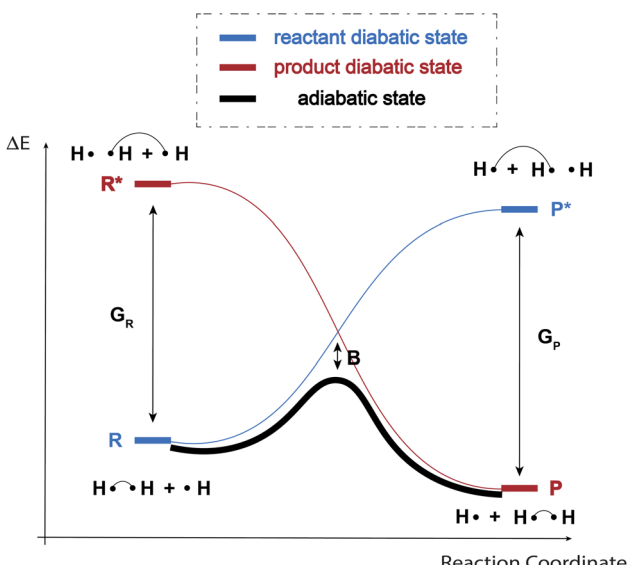


Fig. 1 An example VB reactivity diagram for a model HAT reaction between H_2 and H^+ . Along the reaction coordinate, the reactant diabatic state (blue) rises in energy (since the hydrogen atoms contributing electrons to the formal covalent bond on the left become increasingly separated as the reaction proceeds), the product state (red) drops in energy, since the product covalent bond becomes increasingly stabilized as the associated hydrogens approach. The adiabatic state (black) is the full ground- (or adiabatic) state resulting from the mixing of the localized diabatic states.



The discussion in the previous paragraphs provides us with an ideal QM descriptor representation that should render the mapping function from reaction to HAT barriers as linear as possible. As already indicated in the introduction, computing this complete input representation would be complex and expensive – many different DFT calculations would be needed (for both charged and uncharged species) for every data point. At the same time, the literature suggests that even a subset of the descriptors mentioned above could be sufficient to build an informative representation: for small subsets of the chemical space we are interested in, various groups have previously constructed effective multivariate linear models, as well as some more advanced architectures (random forests, neural networks, *etc.*) with a subset of the descriptors listed above.^{53,59,60,79}

As already indicated above, encouraged by these findings, we selected the BDE-db dataset as a suitable source of descriptors. This dataset contains (relaxed) BDFEs – at room temperature in the gasphase – and BDEs, (Mulliken) atomic charges, and (Mulliken) spin densities for over 200 000 organic radical compounds.³⁶ Additionally, since accurate geometries are included in this dataset, we were able to expand this descriptor list with buried volume values at a marginal computational cost. Finally, we also used these geometries to rapidly compute vertical, *i.e.*, frozen or unrelaxed, BDE values at extended tight-binding (xtb) level of theory (these final low-level descriptors were found to be remarkably predictive – even at this low theory level – for activation energies of HAT reactions between P450 enzymes and organic compounds in a recent study by Gingrich *et al.*⁵³ – see the Methodology section for more details).

With this dataset-derived representation selected, we set out to train a surrogate descriptor model, in combination with a top-level reactivity model, to probe HAT reactivity on the fly.

3 Methodology

3.1 Extracting and curating the descriptor data from the BDE-db dataset

As indicated in the introduction, the training data for the surrogate neural network (*vide infra*) was extracted from a dataset recently released by Paton and co-workers,³⁶ consisting of QM properties for radicals and associated closed shell molecules of less than ten heavy atoms, without formal charges on any of the atoms, and containing exclusively C, H, N, and O atoms. We complemented the registered descriptors, *i.e.*, BDFEs, spin densities, and partial charges, with V_{bur} values around the radical site and frozen BDE values computed at GFN2-xTB level of theory. V_{bur} values were computed with the help of the Morfeus package⁸⁰ with a radius of 3.5 Å.⁸¹ Frozen BDEs were computed by re-optimizing the extracted geometries at GFN2-xTB level of theory and then performing single-point calculations on the bond fragments, *i.e.*, the organic radical and a hydrogen radical respectively. In total, the complete set of descriptors could be obtained for 186 240 dissociation reactions in this manner.

The entire dataset in its curated form can be accessed and downloaded from <https://figshare.com/articles/dataset/>

dataset_surrogate_model_cs/24754341. It should be noted that during the preparation of this manuscript, an expanded version of the dataset, covering the elements S, Cl, F, P, Br and I as well was released.⁸² As such, the approach described here could be expanded straightforwardly to a much broader scope of HAT reactions in the near future.

3.2 Generation of the HAT dataset

To enable comparisons between various types of machine learning model architectures, a dataset of HAT reaction profiles was generated by combining multiple bond dissociation reactions included in the BDE-db dataset.

A fully automated reaction profile computation workflow based on autodE⁸³ and Gaussian16 (ref. 84) was set up to generate this dataset, starting from an input list of reaction SMILES. This workflow is analogous to the workflow recently developed for cycloaddition reactions by Stuyver *et al.*,⁸⁵ an in-depth discussion can be found in Section S1 of the ESI.†

It should be noted that around 40 billion HAT reaction SMILES can in principle be constructed by making combinations between bond dissociation reactions in the BDE-db dataset. Most of these reactions are very similar, involving HAT among two carbon atoms. We aimed to select a tiny sample (2000 reactions) from this huge search space, covering maximal structural diversity, to compute explicitly. To this end, we iteratively sampled enumerated reactions in such a way that the differential reaction fingerprint (radius = 3; nbits = 2048)⁸⁶ distances with all previously sampled reactions exceeded 0.85 (see Section S1† for more details).⁸⁷

As the level of theory for the DFT calculations, we selected M06-2X/def2-SVP^{88,89} for optimizations and frequency calculations, *i.e.*, thermal corrections. Single-point energy refinements were performed at M06-2X/def2-TZVP^{88,90} level of theory. The choice for the functional and basis set was inspired by the benchmarking results from Paton *et al.*⁹¹

One technical aspect where we decided to deviate in our workflow from the previous work on cycloaddition reactions is the conformer selection.⁸⁵ Previously, the default number of conformers in autodE (300) would be generated for every species along the profile, a root mean squared deviation (RMSD) threshold of 0.3 Å would then be applied to remove very similar conformer geometries, after which the lowest energy conformer, computed at GFN2-xTB level of theory, would be selected. Remarkably, for HAT reactions, this methodology leads to poor reproducibility of the activation energies (mean absolute errors between successive runs on 30 randomly sampled reactions amounting to more than 2.1 kcal mol⁻¹ for the activation energy, and ~0.5 kcal mol⁻¹ for the reaction energy; *cf.* Section S1†). After some benchmarking, we adapted these conformer selection settings, selecting 1000 conformers for every species, using an RMSD cut-off of 0.1 Å, and ranking conformers based on single-point M06-2X/def2-SVP^{88,89} energies. In this manner, two successive runs of the workflow on the same set of reaction SMILES result in an acceptable mean absolute error (MAE) of ~1 kcal mol⁻¹ for the activation energies and ~0.6 kcal mol⁻¹ for the reaction energies.



Tunneling corrections were computed based on the semi-classical approximation.⁹² In this approximation, the potential energy barrier is approximated by an Eckart potential, for which the tunneling probability is computed analytically and the tunneling transmission coefficient is integrated numerically. More details can be found in Section S1† and ref. 92.

In total, 1511 reaction profiles were successfully computed in this manner (75.6% success rate).

3.3 Surrogate neural network model for QM descriptor prediction

A graph neural network (GNN), consisting of a directed message-passing neural network (D-MPNN) encoder and a feed-forward neural network (FFNN), was selected for the fast prediction of the QM descriptors.^{20,24} The model architecture is an adaptation of the Chemprop model.²⁰ Inference for an individual molecule starts by parsing its SMILES string, after which a graph-based input representation is constructed, with atoms as nodes and bonds as edges. The D-MPNN module subsequently encodes this molecular graph, resulting in learned atom and bond features. Finally, the learned representation of the molecule is used as input to the multitask FFNN, which yields the final predictions (*cf.* Fig. 2). A more detailed description of the model architecture can be found in Section S2 of the ESI.†

The surrogate model is trained to predict two atom-level descriptors (atomic Mulliken charges and spin densities), as well as three molecule-level descriptors (relaxed BDFEs, frozen BDEs, and V_{bur} of the radical sites). Based on a hyperparameter grid search, the depth was set to 5 for the D-MPNN and 4 for the FFNN. For the hidden size, 1200 neurons were selected for the D-MPNN and 900 for the FFNN (*cf.* Section S2.1 in the ESI†).

Once a reasonable set of hyperparameters was selected, the model was trained on a new data split, where all the radical species and molecules present in the constructed HAT reactivity dataset (*vide supra*) constitute the test set, and the remaining points are split between training (80%) and validation (20%) set.

3.4 Model architecture for the reactivity prediction

Various established model architectures for reactivity prediction have been considered, ranging from linear multivariate regression, k -nearest neighbors (KNN), random forests (RF), graph neural networks (GNN), XGBoost and FFNN, to geometry-based kernel ridge regression (KRR). An in-depth discussion of

the characteristics of each model considered can be found in Sections S3.1 and S3.2 of the ESI.†

Additionally, a couple of models inspired by “delta machine learning” (Δ-ML),^{93–95} were also designed. In this model architecture, the BDFE values, inferred by the surrogate model, are first used to generate an estimated thermodynamic driving force, and this driving force is correlated with the activation energy across the training set. Subsequently, an ML model is trained to predict the deviation of the activation energy, *i.e.*, the target considered in this study, from the established thermodynamic-kinetic correlation trend line. For a more in-depth discussion of this model architecture, we refer to Section S3.3 of the ESI.†

3.5 Datasets

In total, 3 application domains have been considered to showcase the ability of our model architectures to efficiently learn barrier heights in various settings.

In the first application domain, we focused on HAT predictions related to chemical synthesis. We started by analyzing a dataset consisting of 238 computed reaction profiles for alkoxy radicals abstracting hydrogens from hydrocarbons and hetero-substituted compounds in an acetonitrile solution.⁷⁹ Geometry optimizations and frequency calculations were performed at ωB97X-D/6-31G(d) level of theory,^{96–99} single-point energy refinements at UωB97X-D/6-311++G(d,p) level of theory, and solvation was taken into account through the SMD model.¹⁰⁰ Since two of the radicals involved in this dataset contain Cl and F atoms – elements that are not present in the training data of the surrogate model – we computed the descriptors for these species explicitly.

Subsequently, we considered a small dataset of experimentally reported selectivities for 6 hydrocarbons by $\text{CH}_3\text{O}^{\cdot}$ determined by Zuo *et al.*⁵⁷ More specifically, we aimed to reproduce the observed selectivities by inferring the relative barrier heights associated with individual carbon attack positions (15 in total).

A second main dataset within this domain, consisting of reactions associated with photoredox-mediated HAT catalysis, was also considered. 564 reactions with various allylic, propargylic, benzylic, aldehyde and alkyl substrates (resulting in a collection of 182 distinctive C–H bonds positions) and O/N-based radical species, were extracted from the recently

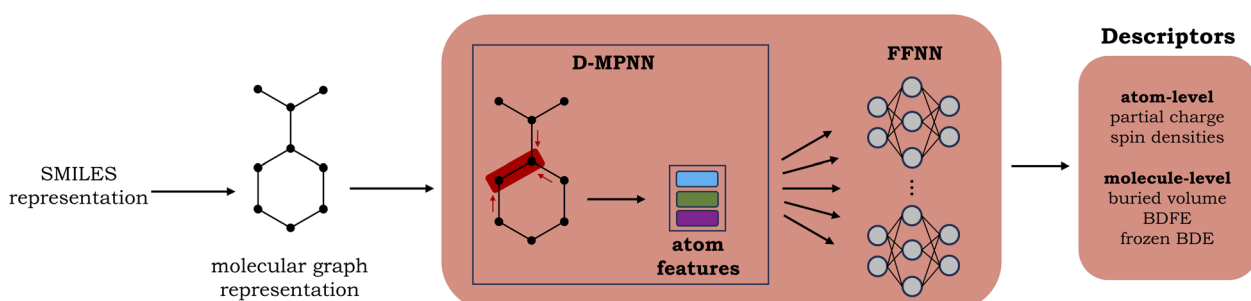


Fig. 2 Schematic representation of the surrogate model used for the QM descriptor predictions.



published dataset by Yang *et al.*⁶⁰ The original computations of the activation energies were performed at B3LYP/6-31+G(d,p)//M06-2X/TZVPP;^{88,89,101–103} solvation energy corrections were included using the SMD model with M06-2X/6-31G(d) in acetonitrile.¹⁰⁰

Finally, we aimed to apply our models to an experimental dataset of rate constants/activation energies for 45 HAT reactions from C(sp³)-H bonds by cumyloxy radical (CumO[·]), compiled by Bietti *et al.*⁶²

In a second application domain, we focused on the prediction of metabolites of medicinally relevant compounds. As such, we considered a second dataset consisting of 24 activation energies for hydrogen atom transfer by the cytochrome P450 enzyme from organic compounds,⁵³ computed at B3LYP/6-311++G(2d,2p)//B3LYP/6-31G(d) (Fe=SVP) level of theory.^{101–103} 5 of the HAT reactions involve compounds with elements outside of the domain of the training data of our surrogate model and hence were discarded in our analysis. The models trained on the resulting extremely small dataset were subsequently applied to predict activation energies for 6 additional computed HAT reaction profiles for unseen substrates.

As a third application, we focus on HAT reactions encountered in atmospheric chemistry. To this end, around 300 HAT reactions were extracted from RMechDB. RMechDB is a database consisting of elementary radical reactions recently assembled by Tavakoli *et al.*⁴⁵ In its current form, the dataset is dominated by gas-phase reactions of isoprene and other organic molecules. No labels, *i.e.*, computed or predicted activation energies, are available for the reactions in this database, and hence we computed reaction profiles ourselves with the same

high-throughput workflow used to generate the previously discussed in-house HAT dataset.

A summary with the main information of every dataset can be found in the Table 2.

4 Results and discussion

4.1 Performance of the surrogate model

In Fig. 3, the performance of the trained surrogate model on the held-out test set, *i.e.*, the radicals and closed-shell molecules present in the BDE-db dataset, is presented. For (relaxed) BDFEs, atomic charges, spin densities, and buried volumes, excellent correlations between predicted and computed values are obtained ($R^2 \geq 0.97$); for frozen BDEs, the correlation is slightly worse ($R^2 = 0.89$), but the quantitative trends are still largely retained.

4.2 Predicting activation energies for our in-house generated dataset

With a performant surrogate model at our disposal, we turned to the in-house generated HAT dataset. In Fig. 4, the distribution of the computed activation and reaction energies, as well as the correlation between both quantities, is presented. Remarkably, activation and reaction energies only correlate moderately ($R^2 = 0.71$), indicating that the Bell–Evans–Polanyi principle^{104,105} on its own is not sufficient to fully explain the trends in the activation energies, and that building a predictive model including multiple descriptors is warranted for this dataset.

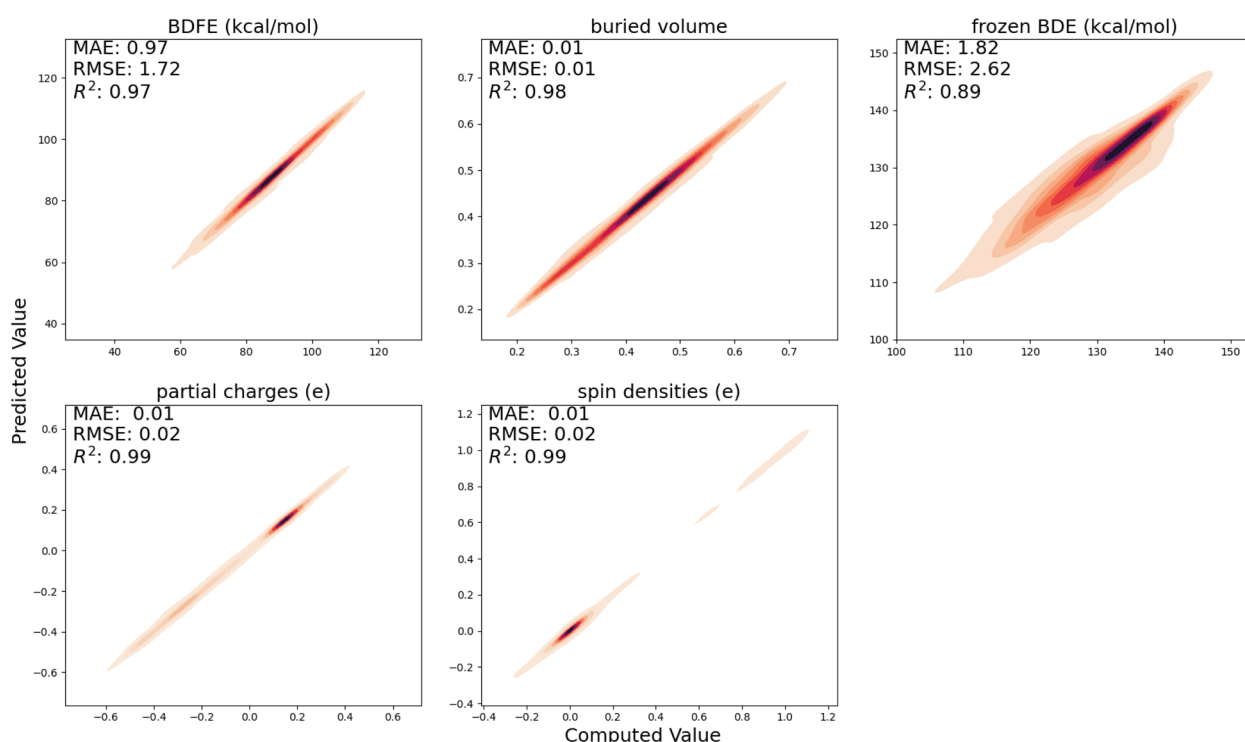


Fig. 3 Correlation between the computed QM descriptors and those predicted by the surrogate model. Note that color brightness is inversely proportional to the density of the points here, *i.e.*, dark patches correspond to a high point density and vice versa.



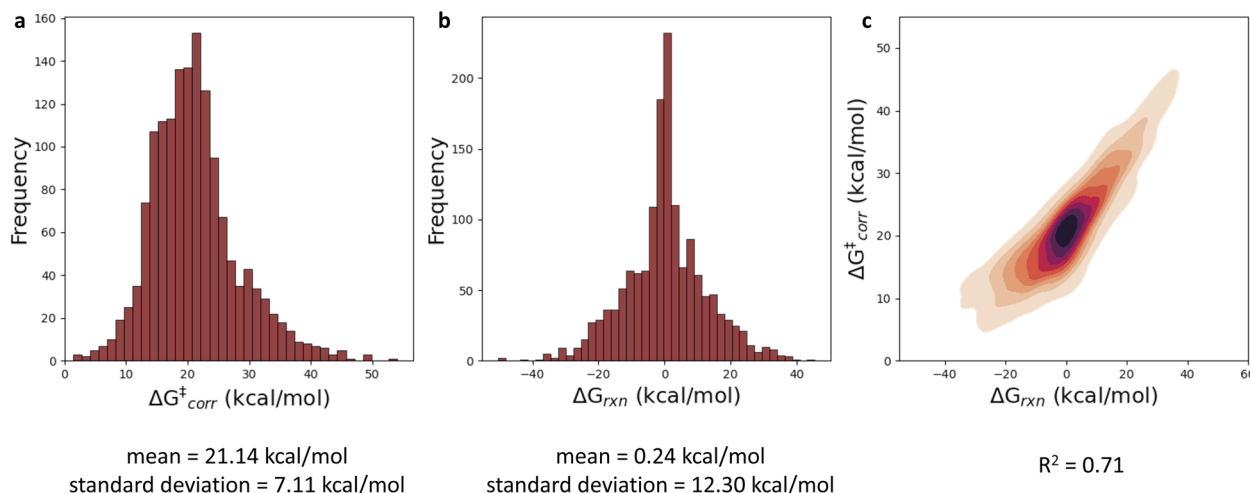


Fig. 4 (a) Histogram presenting the distribution of the computed activation energies with tunneling corrections included ($\Delta G_{\text{corr}}^{\ddagger}$). (b) Histogram representing the distribution of the computed reaction energies (ΔG_{rxn}). (c) Correlation plot between $\Delta G_{\text{corr}}^{\ddagger}$ and ΔG_{rxn} .

Various baseline models, not making use of the informative representation predicted by our surrogate GNN, were considered as baselines. Due to the relatively small size and inherent diversity present in the constructed HAT dataset, all of these model architectures perform remarkably poorly. RF, KNN and XGBoost models taking structural fingerprints, *i.e.*, differential reaction fingerprints (DRFP), as input, reach a mean absolute error (MAE) of 5.2–5.3 kcal mol^{−1} (corresponding to R^2 around 0) in 10-fold cross-validation. This is barely any better than the standard deviation (7 kcal mol^{−1}), *i.e.*, the hypothetical accuracy that would be obtained for a model that always predicts the mean value for the dataset. The GNN architectures tested – a Weisfeiler–Lehmann (WL) one and Chemprop – perform somewhat better, but the MAE still amounts to ∼2.9–3.5 kcal mol^{−1} ($R^2 \sim 0.65$). The geometry-based kernel ridge regression model, based on the recently introduced bond-based reaction representation ($B^2R_i^2$) reaches a similar performance (MAE = 3.55 kcal mol^{−1}).¹⁰⁶

The results quoted above are in great contrast to the results obtained when the predicted informative representation is used as the input for the reactivity model. Now, the MAEs amount to 1.9–2.3 kcal mol^{−1} (*cf.* Table 1) and the corresponding R^2 scores

amount to 0.80–0.85. There is still some non-linearity present in the relationship between the representation used and the activation energies but only to a limited extent: our best non-linear model architecture, the FFNN model, outperforms a multivariate linear regression model by only 0.30 and 0.36 kcal mol^{−1}, in terms of MAE and RMSE, respectively (ensembling 4 FFNNs, the error can be reduced further by 0.02 and 0.03 kcal mol^{−1} respectively). In line with this observation, we also observe that fairly few data points are needed to reach this accuracy; already with 800 training points, the final accuracy is approached within 0.1 kcal mol^{−1} for most of the machine learning model architectures (Fig. 5). Reducing the training set size, the multivariate linear model takes over as the most accurate model when fewer than 400 training points are considered.

As discussed in Section S3.3 of the ESI,† Δ -ML models perfectly adhere to the trends established above. Because of the introduced thermodynamic-kinetic coupling, these models exhibit a better baseline, but we observe again that the accuracy improves significantly when switching from a fingerprint-based input to our surrogate-based informative representation (the MAE reduces from 2.84 to 1.97 kcal mol^{−1}). Since the best Δ -ML does not outperform our regular FFNN, we decided to focus on the non-delta learning models in the remainder of this work.

In Fig. 6a, a schematic overview of the impact of the individual descriptors of the (predicted) informative representation on the accuracy of the multivariate linear model is provided. Our analysis indicates that each descriptor has at least some predictive power, *i.e.*, they all correlate to some extent with the activation energies, so that the prediction accuracy for the corresponding univariate linear regression models exceeds the standard deviation across the dataset by a non-negligible margin. As could have been expected from the Bell–Evans–Polanyi analysis in Fig. 4, the (relaxed) BDFE values correlate extremely well; a linear regression model based exclusively on this (predicted) descriptor reaches an MAE of 2.84 kcal mol^{−1}, which is not dramatically worse than the multivariate model based on all (predicted) descriptors. The descriptor that is most

Table 1 A summary of the performance of some of the model architectures tested on the prediction of ΔG^{\ddagger} for the HAT dataset

Model architecture	MAE (kcal mol ^{−1})	RMSE (kcal mol ^{−1})
RF (fingerprint input)	5.25	6.96
XGBoost (fingerprint input)	5.32	7.03
Chemprop (CGR representation)	2.94	4.15
KRR ($B^2R_i^2$ representation)	3.55	4.71
Linear model (descriptor input)	2.28	3.14
RF (descriptor input)	2.10	3.01
XGBoost (descriptor input)	2.24	3.13
FFNN (descriptor input)	1.98	2.78
Δ -ML (descriptor input)	1.97	2.76

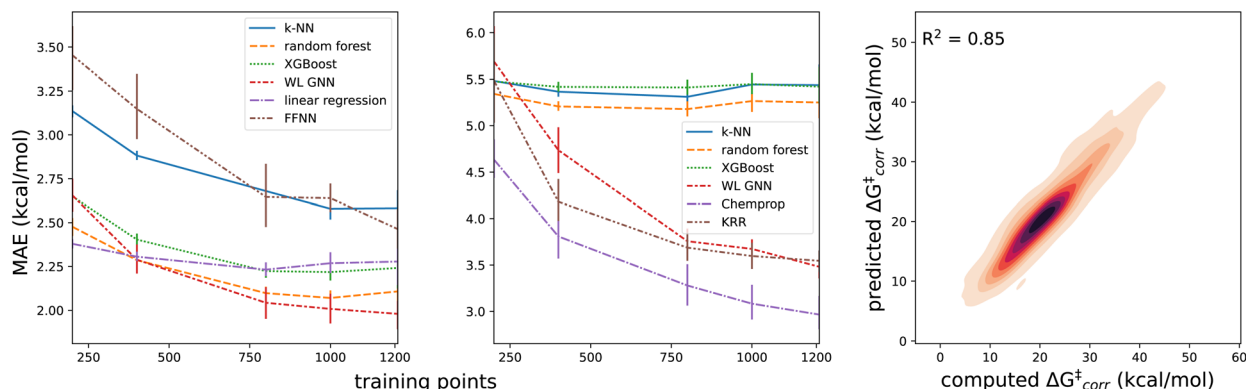


Fig. 5 Learning curves for the ΔG^\ddagger_{corr} for several models based in (a) an intermediate VB learned representation and (b) the differential reaction fingerprints (error bars were determined from the results for the individual folds in the cross-validation). (c) Correlation plot between the computed and predicted activation energies with tunneling corrections ΔG^\ddagger_{corr} for the (in-sample) test sets considered during 10-fold cross-validation for the FFNN model with 4 ensembles. Note that color brightness is inversely proportional to the density of the points here, *i.e.*, dark patches correspond to a high point density and vice versa.

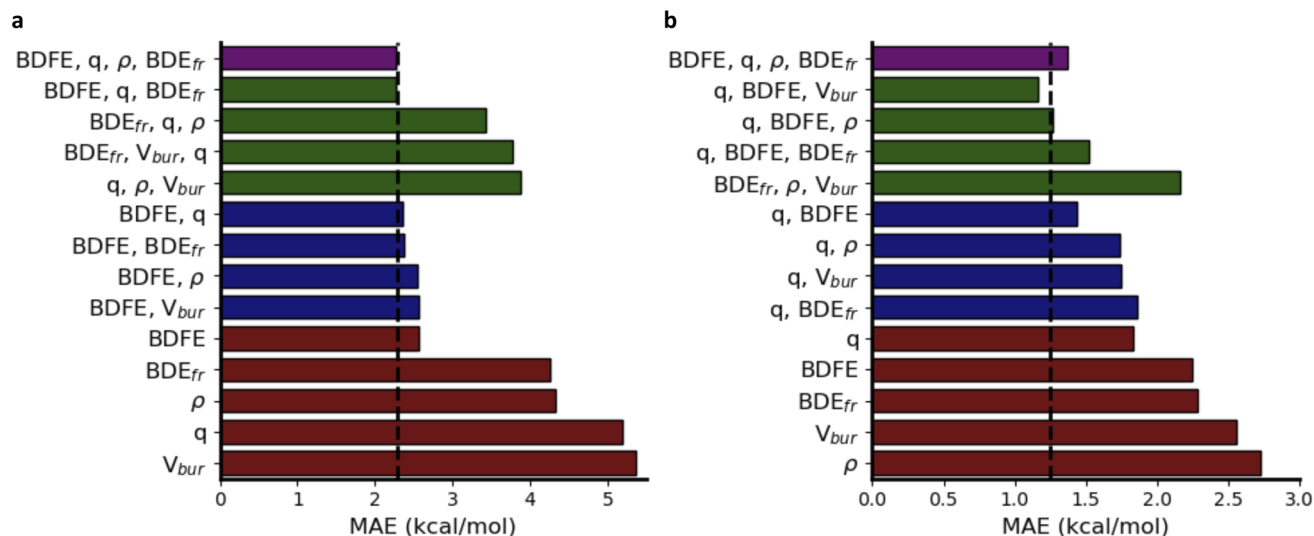


Fig. 6 Performance on ΔG^\ddagger , in terms of mean absolute error (MAE), for multivariate linear models based on a subset of the descriptors. (a) Trained on our in-house HAT dataset. (b) Trained on the 238 reactions involving alkoxy radicals abstracting hydrogens.

complementary to the BDDE, *i.e.*, the descriptor whose inclusion in the linear model reduces the prediction errors the most, is the atomic charge (q), closely followed by the frozen bond dissociation energy (BDE_{fr}). On their own, the spin density (ρ) values on the radical centers of reactants and products, also have significant predictive power, but they do not improve the model accuracy when the BDDE is already considered as an input descriptor. Note that this is in line with the point of view discussed above that changes in delocalization are fully encoded in the thermodynamic driving force: the information encoded in the spin densities overlaps with the information gained from consideration of the BDDE values.⁷³ Remarkably, and in contrast to the results obtained for the smaller subsets of chemical space considered as part of the applications (*vide infra*), the inclusion of V_{bur} does not improve the prediction accuracy on this dataset.

4.3 Applications

In this final section, we will showcase the usefulness of our approach by considering a set of applications. Particularly, we will exploit the data efficiency of models based on our VB-inspired representation to learn activation energies across some extremely small HAT datasets found in the literature (*vide supra*).

As indicated above, the first application area focuses on HAT predictions related to chemical synthesis. More specifically, we started by considering a HAT dataset involving alkoxy radicals and hydrocarbons/heterosubstituted compounds (*cf.* “alkoxy dataset” entry in Table 2).⁷⁹ In previous work, an empirical model based on five computed parameters, respectively describing the electronegativities and delocalization of the reactants and products, as well as the thermodynamic driving force, was proposed.⁵⁹ Applying this empirical model to the full



Table 2 A summary of the different applications and datasets (μ = mean and σ = standard deviation). The tabulated MAE and RMSE values correspond to the best models developed for each dataset respectively

Dataset	Samples	μ (σ) (kcal mol $^{-1}$)	MAE (RMSE) (kcal mol $^{-1}$)
In-house dataset	1511	21.14 (7.11)	1.95 (2.75)
Alkoxy dataset ⁷⁹	238	12.49 (2.78)	1.11 (1.32)
Exp. alkoxy ⁵⁷	15	14.53 (2.16)	0.97 (1.27)
Photoredox HAT ⁶⁰	564	16.39 (4.87)	0.94 (1.42)
Exp. cumyloxy ⁶²	45	12.82 (1.49)	1.04 (1.26)
Cytochrome P450 (ref. 53)	19	12.91 (1.65)	0.94 (1.01)
Atmospheric HAT ⁴⁵	73	9.10 (5.29)	1.20 (1.57)

dataset, an MAE 0.85 kcal mol $^{-1}$ ($R^2 = 0.84$) is obtained on the training set, and 1.24 kcal mol $^{-1}$ ($R^2 = 0.72$) on the test set.

With the help of our on-the-fly predicted VB-inspired representation, MAEs of 1.02 kcal mol $^{-1}$ ($R^2 = 0.76$) and 1.25 kcal mol $^{-1}$ ($R^2 = 0.66$) are reached, respectively on the training and test set, with a simple multivariate linear model. Even though our linear regression model does not outperform the tailored, empirical expression by Liu *et al.*⁵⁹ here, it is important to note that our predictions can be performed on a millisecond scale, whereas the computed descriptor inputs needed in the empirical model require geometry generation and a succession of tedious DFT calculations.

We also considered the performance of non-linear model architectures on this small dataset. Training a FFNN from scratch results in an MAE on the test set of 1.66 kcal mol $^{-1}$ ($R^2 = 0.45$). Taking a transfer learning approach, *i.e.*, using the parameters from the FFNN model trained on the more extensive and diverse in-house HAT dataset to initialize the network, an MAE of 1.22 kcal mol $^{-1}$ ($R^2 = 0.68$) is reached on the test set; already marginally better than the linear model. Remarkably, an RF model based on the predicted representation now actually outperforms all other model architectures, with an MAE of 1.11 kcal mol $^{-1}$ ($R^2 = 0.78$).

Another remarkable observation is that the predictive power of the respective descriptors in our VB-inspired representation has changed significantly upon switching from the in-house HAT dataset, discussed in the previous section, to the current one (Fig. 6; *cf.* Section S5.2 in the ESI†). As mentioned before, in the diverse dataset constructed as part of this study, the inclusion of the predicted BDFEs reduced the MAE of the linear model the most, and the inclusion of V_{bur} had no observable effect on the model accuracy. In the small alkoxy radical dataset, however, BDFE values are not nearly as predictive. Atomic charges improve the model accuracy the most now, and the inclusion of V_{bur} leads to significant further improvements. These differences can be connected to the more pronounced polar effects in alkoxy radicals, due to the involvement of a more electronegative radical center.^{65,107–109} In more general terms, these findings about descriptor importance underscore that local correlations in small subsections of chemical space are not necessarily transferable and that caution is needed when

aiming to draw universal conclusions about reactivity trends based purely on empirical trends.

Next, we attempted to predict the experimentally reported HAT selectivities reported by Zuo *et al.*⁵⁷ which were subsequently computationally recovered through DFT calculations by Ma and co-workers (*cf.* “Exp. alkoxy” entry in Table 2).⁷⁹ In Fig. 7, the performances of the various model architectures are presented. For all models, the predictions are in qualitative agreement with the experimentally observed regioselectivity the majority of the time, with the RF and FFNN models each reaching 5 out of 6 correct predictions. Also quantitatively, our models reach good accuracy as compared to the computed DFT barriers in this application. The most accurate model is the FFNN (MAE = 0.97 kcal mol $^{-1}$, RMSE = 1.27 kcal mol $^{-1}$, $R^2 = 0.63$).

Subsequently, we focus on the dataset of photoredox C–H bond functionalization reactions generated by Yang *et al.* (*cf.* “photoredox HAT” entry in 2).⁶⁰ On the full dataset of 500+ reactions, our approach results in excellent accuracy, regardless of the secondary reactivity model architecture (for the FFNN, an MAE of 1.06 kcal mol $^{-1}$ and R^2 of 0.90 is reached in 5-fold cross-validation, and for the RF, an MAE of 0.94 kcal mol $^{-1}$ and R^2 of 0.91 is obtained). It should be noted that with a heavily fine-tuned input representation of over 50 explicitly computed QM descriptors in combination with AdaBoost, Yang *et al.*⁶⁰ achieved an even higher accuracy in the original work on this dataset (MAE = 0.64 kcal mol $^{-1}$ and $R^2 = 0.96$ in 5-fold cross-validation). Reducing the training set size to 25–50 data points causes this advantage compared to our models to vanish (see Section S6 in the ESI†), underscoring the merit of our approach in the extremely low data regime.

To end this first application area, we considered the experimental dataset of 45 HAT activation energies, assembled by Bietti and co-workers⁶² (*cf.* “Exp. cumyloxy” entry in Table 2). Our models, trained on the photoredox dataset specified above, predict the (rescaled) activation energies in this experimental set with good accuracy (\sim 1 kcal mol; *cf.* Section S5.3 of the ESI†), correctly identifying all of the reaction barriers to be low. However, the coefficients of determination, *i.e.*, the extent to which fine-grained trends across these 45 reactions are recovered, are essentially zero. The main reason for this failure to recover the reactivity trends is the distinct data distribution, *i.e.*, the activation energies in this specific experimental dataset are “outliers” with respect to the reactions present in Ma *et al.*’s⁷⁹ dataset, and – to a lesser extent – the fairly low spread in the targets (the standard deviation amounts to only 1.5 kcal mol $^{-1}$). This conjecture can be confirmed by retraining our models on the 45 data points by Bietti *et al.*: in 10-fold cross-validation (*i.e.*, when only 36 in-distribution training points are considered), a significantly better $R^2 = 0.44$ is now reached for our best model, the ensembled FFNN with transfer learning.

The second application area focuses on P450 metabolism of medicinally relevant compounds (*cf.* “Cytochrome P450” entry in Table 2). As discussed in the Methodology section, predictive models were trained on a tiny dataset of 19 HAT activation energies, and subsequently, these models were applied to predict 6 barriers for unseen substrates, in line with the work by



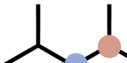
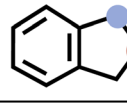
Molecule	Exp ratio	DFT	Linear regression	Random Forest	FFNN
	97	12.47	13.35	12.97	12.99
	3	17.28	16.55	16.90	17.03
	47	14.34	13.38	14.79	14.01
	48	14.05	13.73	14.14	13.86
	5	17.56	16.25	17.16	16.75
	-	17.23	16.78	15.58	17.13
	-	15.62	17.92	14.40	17.31
	1	13.35	15.31	14.79	15.07
	22	14.97	9.60	14.36	12.98
	78	13.01	21.59	14.02	15.25
	14	15.71	15.04	14.47	15.00
	77	12.10	13.47	12.62	13.11
	9	16.87	16.06	16.95	16.98
	1	10.49	11.73	13.88	12.68
	-	12.84	13.11	14.37	14.11

Fig. 7 Prediction of selectivity and ΔG^\ddagger for the compounds experimentally considered by Zuo *et al.*⁵⁷ for the various model architectures trained on the alkoxy radical dataset. Bold values represent the major regioisomer.

Gingrich *et al.*⁵³ We again started with a multivariate linear regression model, but we considered only (a subset of) the descriptors of the hydrocarbons to reduce collinearity and avoid overfitting (Section S6†). With the trained model, based only on the predicted spin density and buried volume, an MAE of 1.12 kcal mol⁻¹ is obtained for the unseen substrates, in line with the accuracy reached by the predictive model proposed by Gingrich *et al.* (1.15 kcal mol⁻¹).⁵³ Adding more descriptors, the MAE of the model increases (Section S7†).

Subsequently, we also considered our FFNN architecture. Trained from scratch on the same subset of descriptors with two neurons, the model reaches an MAE of 1.04 kcal mol⁻¹. With 4 ensembles, the model reaches an MAE of 0.94 kcal mol⁻¹.

For the final application, we considered the HAT reactions found in RMechDB (Section S8 of the ESI†). In total, we were able to extract 268 reactions, falling within the scope of our surrogate model, from this database; primarily HAT reactions between organic compounds and HO[·] and HOO[·] radicals, *i.e.*, the onset of atmospheric oxidation. With our autodE-based workflow for reaction profile computation, we only managed to successfully compute profiles for 73 of these reactions (failure

sources are detailed in Section S8;† see also “atmospheric HAT” entry in Table 2).

At first, we tried to directly reproduce the computed activation energies with the predictive models trained on our in-house assembled HAT dataset, but even our best model (ensembled FFNN) reached an inadequate MAE of 4.58 kcal mol⁻¹ (RMSE = 5.11 kcal mol⁻¹, R^2 = 0.05). A reasonable explanation for this poor performance is (once again) the distribution of the data: our in-house generated dataset contained no examples involving HO[·] or HOO[·] radicals, and the activation energies for the reactions extracted from RMechDB (mean $\Delta G_{\text{corr}}^\ddagger$ = 9.10 kcal mol⁻¹) tend to be at the lower edge of the activation energy distribution of our training data (*cf.* Fig. 4). Once more, upon re-training on the 73 computed RMechDB reaction profiles, an outstanding accuracy is recovered; in 10-fold cross-validation, our ensembled FFNN with transfer learning now reaches R^2 = 0.88 (MAE = 1.29 kcal mol⁻¹, RMSE = 1.51 kcal mol⁻¹); our multivariate linear model reaches R^2 = 0.88 as well (MAE = 1.20 kcal mol⁻¹, RMSE = 1.57 kcal mol⁻¹). With both of these fine-tuned models, we made predictions for the remaining reactions extracted from



the database (cf. https://github.com/chimie-paristech-CTM/energy_predictor_HAT/tree/master/reactivity_model/RMechDB_pred).

The observations for this last application are yet another illustration that setting up a machine learning model for chemical reactivity, able to generalize across application domains, is hard and data-intensive, but that introducing QM-based descriptors in the model architecture – particularly in combination with transfer learning – can remedy this situation to a large extent.

5 Conclusions

The poor data-efficiency of generic machine learning models poses a major challenge to their application in chemical reactivity studies, since for most specialized predictive tasks in this domain, only limited training data is available. In this work, we have explored a strategy to make machine learning workflows for reactivity prediction significantly less data-hungry, by making use of an intermediate informative reaction representation. This informative representation was constructed based on a VB analysis for generic HAT reactions. A surrogate model, able to predict (most of) the identified quantum chemical informative descriptors was subsequently built based on a repurposed, publicly available dataset of descriptors and geometries of organic radicals. Combining the surrogate model with a secondary reactivity model, we achieved unequivocally superior performance on a medium-sized, in-house generated, dataset of DFT computed reaction profiles of diverse HAT reactions, compared to any other machine learning approach we tried. Because of the extreme data efficiency of our descriptor-augmented models, we were able to demonstrate that they can be fine-tuned and applied to small datasets across various reaction conditions, settings, and application domains, ranging from regular (liquid phase) synthesis, over metabolism and drug design, to atmospheric chemistry.

The presented modular approach towards reactivity prediction has the potential to significantly expand the scope of machine learning workflows for focused reactivity predictions, as long as the reactivity type is qualitatively understood and can be modeled accurately, and high-quality descriptor datasets are available for surrogate model training. In this context, it is crucial to emphasize the necessity for careful curation of these property datasets, ensuring that the chosen descriptors are pertinent, *i.e.*, relevant, to a diverse array of reaction types.

Data availability

The code used to generate/curate the different datasets as well as to generate the baseline modes can be found at https://github.com/chimie-paristech-CTM/bde_hat. The code associated with the final reactivity model, *i.e.*, the surrogate model in combination with an FFNN, can be found at https://github.com/chimie-paristech-CTM/energy_predictor_HAT, a script to generate the main results reported in this paper can also be found there. The (generated/curated) datasets can be downloaded at <https://figshare.com/projects/>

[Hydrogen_atom_transfer_reactions/188007](#) and https://figshare.com/articles/dataset/dataset_surrogate_model_cs/24754341 respectively.

Author contributions

JEAR: data curation, software, methodology, formal analysis, visualization, writing. RMN: software, methodology, writing (review), visualization. TS: conceptualization, methodology, formal analysis, writing, supervision, funding acquisition.

Conflicts of interest

There are no conflicts to declare.

Acknowledgements

JEAR and TS acknowledge the French National Agency for Research (ANR) for a CPJ grant (ANR-22-CPJ1-0093-01). This work was granted access to the HPC resources of IDRIS under the allocation 2023-100732 granted by GENCI. RMN thanks the Zeno Karl Schindler Foundation for their generous financial support, and Connor Coley and Gisbert Schneider for their guidance during her Master's thesis work.

Notes and references

- 1 C. W. Coley, R. Barzilay, T. S. Jaakkola, W. H. Green and K. F. Jensen, *ACS Cent. Sci.*, 2017, **3**, 434–443.
- 2 C. W. Coley, W. Jin, L. Rogers, T. F. Jamison, T. S. Jaakkola, W. H. Green, R. Barzilay and K. F. Jensen, *Chem. Sci.*, 2019, **10**, 370–377.
- 3 P. Schwaller, T. Laino, T. Gaudin, P. Bolgar, C. A. Hunter, C. Bekas and A. A. Lee, *ACS Cent. Sci.*, 2019, **5**, 1572–1583.
- 4 C. W. Coley, L. Rogers, W. H. Green and K. F. Jensen, *ACS Cent. Sci.*, 2017, **3**, 1237–1245.
- 5 Y. Wang, C. Pang, Y. Wang, J. Jin, J. Zhang, X. Zeng, R. Su, Q. Zou and L. Wei, *Nat. Commun.*, 2023, **14**, 6155.
- 6 L. Fang, J. Li, M. Zhao, L. Tan and J.-G. Lou, *Nat. Commun.*, 2023, **14**, 2446.
- 7 A. Tripp, K. Maziarz, S. Lewis, M. Segler and J. M. Hernandez-Lobato, *Retro-fallback: retrosynthetic planning in an uncertain world*, 2023.
- 8 D. Weininger, *J. Chem. Inf. Comput. Sci.*, 1988, **28**, 31–36.
- 9 M. S. Sigman, K. C. Harper, E. N. Bess and A. Milo, *Acc. Chem. Res.*, 2016, **49**, 1292–1301.
- 10 A. F. Zahrt, J. J. Henle, B. T. Rose, Y. Wang, W. T. Darrow and S. E. Denmark, *Science*, 2019, **363**, eaau5631.
- 11 D. T. Ahneman, J. G. Estrada, S. Lin, S. D. Dreher and A. G. Doyle, *Science*, 2018, **360**, 186–190.
- 12 W. Beker, E. P. Gajewska, T. Badowski and B. A. Grzybowski, *Angew. Chem., Int. Ed.*, 2019, **58**, 4515–4519.
- 13 K. Jorner, T. Brinck, P.-O. Norrby and D. Buttar, *Chem. Sci.*, 2021, **12**, 1163–1175.
- 14 X. Li, S.-Q. Zhang, L.-C. Xu and X. Hong, *Angew. Chem., Int. Ed.*, 2020, **59**, 13253–13259.





15 D. F. Nippa, K. Atz, R. Hohler, A. T. Müller, A. Marx, C. Bartelmus, G. Wuitschik, I. Marzuoli, V. Jost, J. Wolfard, *et al.*, *Enabling late-stage drug diversification by high-throughput experimentation with geometric deep learning*, 2022.

16 K. Low, M. L. Coote and E. I. Izgorodina, *J. Chem. Theory Comput.*, 2023, **19**, 1466–1475.

17 K. Low, M. L. Coote and E. I. Izgorodina, *J. Chem. Theory Comput.*, 2022, **18**, 1607–1618.

18 K. Low, R. Kobayashi and E. I. Izgorodina, *J. Chem. Phys.*, 2020, **153**, 104101.

19 J. G. Estrada, D. T. Ahneman, R. P. Sheridan, S. D. Dreher and A. G. Doyle, *Science*, 2018, **362**, eaat8763.

20 K. Yang, K. Swanson, W. Jin, C. Coley, P. Eiden, H. Gao, A. Guzman-Perez, T. Hopper, B. Kelley, M. Mathea, *et al.*, *J. Chem. Inf. Model.*, 2019, **59**, 3370–3388.

21 Z. Liu, L. Lin, Q. Jia, Z. Cheng, Y. Jiang, Y. Guo and J. Ma, *J. Chem. Inf. Model.*, 2021, **61**, 1066–1082.

22 R. Zubatyuk, J. S. Smith, J. Leszczynski and O. Isayev, *Sci. Adv.*, 2019, **5**, eaav6490.

23 K. T. Schütt, H. E. Sauceda, P.-J. Kindermans, A. Tkatchenko and K.-R. Müller, *J. Chem. Phys.*, 2018, **148**, 241722.

24 Y. Guan, C. W. Coley, H. Wu, D. Ranasinghe, E. Heid, T. J. Struble, L. Pattanaik, W. H. Green and K. F. Jensen, *Chem. Sci.*, 2021, **12**, 2198–2208.

25 W. Jin, C. Coley, R. Barzilay and T. Jaakkola, *Adv. Neural. Inf. Process. Syst.*, 2017, **30**, 2607–2616.

26 G. F. von Rudorff, S. N. Heinen, M. Bragato and O. A. von Lilienfeld, *Mach. Learn.: Sci. Technol.*, 2020, **1**, 045026.

27 S. Heinen, G. F. von Rudorff and O. A. von Lilienfeld, *J. Chem. Phys.*, 2021, **155**, 064105.

28 T. Stuyver and C. W. Coley, *J. Chem. Phys.*, 2022, **156**, 084104.

29 M. A. Lim, S. Yang, H. Mai and A. C. Cheng, *J. Chem. Inf. Model.*, 2022, **62**, 6336–6341.

30 A. Gaulton, L. J. Bellis, A. P. Bento, J. Chambers, M. Davies, A. Hersey, Y. Light, S. McGlinchey, D. Michalovich, B. Al-Lazikani, *et al.*, *Nucleic Acid Res.*, 2012, **40**, D1100–D1107.

31 *Pistachio (NextMove Software)*, <https://www.nextmovesoftware.com/pistachio.html>.

32 R. Ramakrishnan, P. O. Dral, M. Rupp and O. A. Von Lilienfeld, *Sci. Data*, 2014, **1**, 1–7.

33 M. Nakata and T. Shimazaki, *J. Chem. Inf. Model.*, 2017, **57**, 1300–1308.

34 M. Nakata, T. Shimazaki, M. Hashimoto and T. Maeda, *J. Chem. Inf. Model.*, 2020, **60**, 5891–5899.

35 A. Stuke, C. Kunkel, D. Golze, M. Todorović, J. T. Margraf, K. Reuter, P. Rinke and H. Oberhofer, *Sci. Data*, 2020, **7**, 58.

36 P. C. St. John, Y. Guan, Y. Kim, B. D. Etz, S. Kim and R. S. Paton, *Sci. Data*, 2020, **7**, 244.

37 C. Isert, K. Atz, J. Jiménez-Luna and G. Schneider, *Sci. Data*, 2022, **9**, 1–11.

38 R. M. Neeser, C. Isert, T. Stuyver, G. Schneider and C. W. Coley, *Chem. Data Collect.*, 2023, **46**, 101040.

39 K. Schütt, P.-J. Kindermans, H. E. Sauceda Felix, S. Chmiela, A. Tkatchenko and K.-R. Müller, *Adv. Neural. Inf. Process. Syst.*, 2017, **30**, 991–1001.

40 J. Gasteiger, S. Giri, J. T. Margraf and S. Günemann, *Fast and uncertainty-aware directional message passing for non-equilibrium molecules*, 2020.

41 G. A. Pinheiro, J. Mucolini, M. D. Soares, R. C. Prati, J. L. Da Silva and M. G. Quiles, *J. Phys. Chem. A*, 2020, **124**, 9854–9866.

42 N. De Cao and T. Kipf, *MolGAN: An implicit generative model for small molecular graphs*, 2018.

43 Y. Bian and X.-Q. Xie, *J. Mol. Model.*, 2021, **27**, 1–18.

44 J. Westermayr, J. Gilkes, R. Barrett and R. J. Maurer, *Nat. Comput. Sci.*, 2023, **3**, 139–148.

45 M. Tavakoli, Y. T. T. Chiu, P. Baldi, A. M. Carlton and D. Van Vranken, *J. Chem. Inf. Model.*, 2023, **63**, 1114–1123.

46 Y. Zhang, J. Yu, H. Song and M. Yang, *Structure-Based Reaction Descriptors for Predicting Rate Constants by Machine Learning: Application to Hydrogen Abstraction from Alkanes by CH₃/H/O Radicals*, 2023.

47 J. Yu, D. Shan, H. Song and M. Yang, *Fuel*, 2022, **322**, 124150.

48 W. Nie, C. Yan, L. Yang, P. Roldin, Y. Liu, A. L. Vogel, U. Molteni, D. Stolzenburg, H. Finkenzeller, A. Amorim, *et al.*, *Nat. Commun.*, 2023, **14**, 3347.

49 L. De Keer, P. Van Steenberge, M.-F. Reyniers, G. Gryn'ova, H. M. Aitken and M. L. Coote, *Polym. Chem.*, 2022, **13**, 3304–3314.

50 G. Gryn'ova, J. L. Hodgson and M. L. Coote, *Org. Biomol. Chem.*, 2011, **9**, 480–490.

51 A. Grinberg Dana, H. Wu, D. S. Ranasinghe, F. C. Pickard IV, G. P. Wood, T. Zelesky, G. W. Sluggett, J. Mustakis and W. H. Green, *Mol. Pharmaceutics*, 2021, **18**, 3037–3049.

52 H. Wu, A. Grinberg Dana, D. S. Ranasinghe, F. C. Pickard IV, G. P. Wood, T. Zelesky, G. W. Sluggett, J. Mustakis and W. H. Green, *Mol. Pharmaceutics*, 2022, **19**, 1526–1539.

53 P. W. Gingrich, J. B. Siegel and D. J. Tantillo, *Chem.: Methods*, 2022, **2**, e202100108.

54 H. Matsubara, T. Kawamoto, T. Fukuyama and I. Ryu, *Acc. Chem. Res.*, 2018, **51**, 2023–2035.

55 S. Sarkar, K. P. S. Cheung and V. Gevorgyan, *Chem. Sci.*, 2020, **11**, 12974–12993.

56 L. Capaldo and D. Ravelli, *Eur. J. Org. Chem.*, 2017, **2017**, 2056–2071.

57 Q. An, Z. Wang, Y. Chen, X. Wang, K. Zhang, H. Pan, W. Liu and Z. Zuo, *J. Am. Chem. Soc.*, 2020, **142**, 6216–6226.

58 Q. An, Y.-Y. Xing, R. Pu, M. Jia, Y. Chen, A. Hu, S.-Q. Zhang, N. Yu, J. Du, Y. Zhang, J. Chen, W. Liu, X. Hong and Z. Zuo, *J. Am. Chem. Soc.*, 2023, **145**, 359–376.

59 F. Liu, S. Ma, Z. Lu, A. Nangia, M. Duan, Y. Yu, G. Xu, Y. Mei, M. Bietti and K. Houk, *J. Am. Chem. Soc.*, 2022, **144**, 6802–6812.

60 L.-C. Yang, X. Li, S.-Q. Zhang and X. Hong, *Org. Chem. Front.*, 2021, **8**, 6187–6195.

61 Y. Sun, F. Liu, J. N. Sanders and K. Houk, *J. Org. Chem.*, 2023, **88**, 12668–12676.

62 M. Salamone, M. Galeotti, E. Romero-Montalvo, J. A. van Santen, B. D. Groff, J. M. Mayer, G. A. DiLabio and M. Bietti, *J. Am. Chem. Soc.*, 2021, **143**, 11759–11776.

63 M. Finn, R. Friedline, N. K. Suleman, C. J. Wohl and J. M. Tanko, *J. Am. Chem. Soc.*, 2004, **126**, 7578–7584.

64 K. R. Korzekwa, J. P. Jones and J. R. Gillette, *J. Am. Chem. Soc.*, 1990, **112**, 7042–7046.

65 B. D. Groff, B. Koronkiewicz and J. M. Mayer, *J. Org. Chem.*, 2023, (88), 16259–16269.

66 J. Han, Y. Kwon, Y.-S. Choi and S. Kang, *J. Cheminf.*, 2024, **16**, 25.

67 S. Shaik and A. Shurki, *Angew. Chem., Int. Ed.*, 1999, **38**, 586–625.

68 S. S. Shaik and P. C. Hiberty, *A chemist's guide to valence bond theory*, John Wiley & Sons, 2007.

69 S. Shaik, D. Kumar and S. P. De Visser, *J. Am. Chem. Soc.*, 2008, **130**, 10128–10140.

70 W. Lai, C. Li, H. Chen and S. Shaik, *Angew. Chem., Int. Ed.*, 2012, **51**, 5556–5578.

71 L. Song, W. Wu, P. C. Hiberty and S. Shaik, *Chem.-Eur. J.*, 2006, **12**, 7458–7466.

72 G. N. Sastry and S. Shaik, *J. Am. Chem. Soc.*, 1998, **120**, 2131–2145.

73 T. Stuyver, F. De Proft, P. Geerlings and S. Shaik, *J. Am. Chem. Soc.*, 2020, **142**, 10102–10113.

74 T. Stuyver, D. Danovich, F. De Proft and S. Shaik, *J. Am. Chem. Soc.*, 2019, **141**, 9719–9730.

75 J. Joy, T. Stuyver and S. Shaik, *J. Am. Chem. Soc.*, 2020, **142**, 3836–3850.

76 J. Li, S. Zhou, J. Zhang, M. Schlangen, T. Weiske, D. Usharani, S. Shaik and H. Schwarz, *J. Am. Chem. Soc.*, 2016, **138**, 7973–7981.

77 T. Stuyver and S. Shaik, *J. Am. Chem. Soc.*, 2020, **142**, 20002–20013.

78 L. C. Gallegos, G. Luchini, P. C. St. John, S. Kim and R. S. Paton, *Acc. Chem. Res.*, 2021, **54**, 827–836.

79 S. Ma, S. Wang, J. Cao and F. Liu, *ACS Omega*, 2022, **7**, 34858–34867.

80 K. Jorner, *Morfeus: Molecular features for machine learning*, 2022, <https://github.com/digital-chemistry-laboratory/morfeus>.

81 S. S. SV, P. C. S. John and R. S. Paton, *Chem. Sci.*, 2021, **12**, 13158–13166.

82 S. S. S. Vejaykummar, Y. Kim, S. Kim, P. S. John and R. Paton, *Expansion of Bond Dissociation Prediction with Machine Learning to Medicinally and Environmentally Relevant Chemical Space*, 2023.

83 T. A. Young, J. J. Silcock, A. J. Sterling and F. Duarte, *Angew. Chem., Int. Ed.*, 2021, **133**, 4312–4320.

84 M. Frisch, G. Trucks, H. Schlegel, G. Scuseria, M. Robb, J. Cheeseman, G. Scalmani, V. Barone, G. Petersson, H. Nakatsuji, et al., *Gaussian 16*, 2016.

85 T. Stuyver, K. Jorner and C. W. Coley, *Sci. Data*, 2023, **10**, 66.

86 D. Probst, P. Schwaller and J.-L. Reymond, *Digital Discovery*, 2022, **1**, 91–97.

87 N. Casetti, J. E. Alfonso-Ramos, C. W. Coley and T. Stuyver, *Chem.-Eur. J.*, 2023, e202301957.

88 Y. Zhao and D. G. Truhlar, *Theor. Chem. Acc.*, 2008, **120**, 215–241.

89 A. Schäfer, H. Horn and R. Ahlrichs, *J. Chem. Phys.*, 1992, **97**, 2571–2577.

90 A. Schäfer, C. Huber and R. Ahlrichs, *J. Chem. Phys.*, 1994, **100**, 5829–5835.

91 P. C. St. John, Y. Guan, Y. Kim, S. Kim and R. S. Paton, *Nat. Commun.*, 2020, **11**, 2328.

92 B. C. Garrett and D. G. Truhlar, *J. Phys. Chem.*, 1979, **83**, 2921–2926.

93 R. Ramakrishnan, P. O. Dral, M. Rupp and O. A. Von Lilienfeld, *J. Chem. Theory Comput.*, 2015, **11**, 2087–2096.

94 T. Bereau, R. A. DiStasio, A. Tkatchenko and O. A. Von Lilienfeld, *J. Chem. Phys.*, 2018, **148**, 241706.

95 M. Bogojeski, L. Vogt-Maranto, M. E. Tuckerman, K.-R. Müller and K. Burke, *Nat. Commun.*, 2020, **11**, 5223.

96 J.-D. Chai and M. Head-Gordon, *Phys. Chem. Chem. Phys.*, 2008, **10**, 6615–6620.

97 J.-D. Chai and M. Head-Gordon, *J. Chem. Phys.*, 2008, **128**, 084106.

98 P. C. Hariharan and J. A. Pople, *Theor. Chim. Acta*, 1973, **28**, 213–222.

99 M. M. Franci, W. J. Pietro, W. J. Hehre, J. S. Binkley, M. S. Gordon, D. J. DeFrees and J. A. Pople, *J. Chem. Phys.*, 1982, **77**, 3654–3665.

100 A. V. Marenich, C. J. Cramer and D. G. Truhlar, *J. Phys. Chem. B*, 2009, **113**, 6378–6396.

101 A. D. Becke, *Phys. Rev. A: At., Mol., Opt. Phys.*, 1988, **38**, 3098.

102 C. Lee, W. Yang and R. G. Parr, *Phys. Rev. B: Condens. Matter Mater. Phys.*, 1988, **37**, 785.

103 P. J. Stephens, F. J. Devlin, C. F. Chabalowski and M. J. Frisch, *J. Phys. Chem.*, 1994, **98**, 11623–11627.

104 R. P. Bell, *Proc. R. Soc. A*, 1936, **154**, 414–429.

105 M. Evans and M. Polanyi, *Trans. Faraday Soc.*, 1936, **32**, 1333–1360.

106 P. van Gerwen, A. Fabrizio, M. D. Wodrich and C. Corminboeuf, *Mach. Learn.: Sci. Technol.*, 2022, **3**, 045005.

107 M. Salamone, F. Basili and M. Bietti, *J. Org. Chem.*, 2015, **80**, 3643–3650.

108 J. M. Tedder, *Angew. Chem., Int. Ed.*, 1982, **21**, 401–410.

109 A. Ruffoni, R. C. Mykura, M. Bietti and D. Leonori, *Nat. Synth.*, 2022, **1**, 682–695.

